coatings

MDPI

Article

Effect of High-Speed Powder Feeding on Microstructure and Tribological Properties of Fe-Based Coatings by Laser Cladding

Qiang Wang [1,2,*], Runling Qian [1], Ju Yang [1], Wenjuan Niu [1], Liucheng Zhou [3], Xinlei Pan [3] and Chengming Su [4]

1 School of Metallurgical Engineering, Xi'an University of Architecture and Technology, Xi'an 710055, China; yangjuzc@163.com (R.Q.); ju.yang@xauat.edu.cn (J.Y.); wenjuan.niu@xauat.edu.cn (W.N.)
2 Shaanxi Research Center of Metallurgical Engineering, Xi'an 710055, China
3 Science and Technology on Plasma Dynamics Laboratory, Air Force Engineering University, Xi'an 710038, China; liucheng.zhou@xauat.edu.cn (L.Z.); xinlei.pan@xauat.edu.cn (X.P.)
4 Shaanxi Tianyuan Intelligent Remanufacturing Co., Ltd., Xi'an 710065, China; chengming.su@xauat.edu.cn
* Correspondence: qiang.wang@xauat.edu.cn

Abstract: In order to improve the wear resistance of 27SiMn steel substrate, Fe-based alloy coatings were prepared by laser cladding technology in the present study. In comparison to the conventional gravity powder feeding (GF) process, high-speed powder feeding (HF) process was used to prepare Fe-based alloy coating on 27SiMn steel substrate. The effect of diversified energy composition of powder materials on the microstructure and properties of coatings were systematically studied. X-ray diffractometer (XRD), optical microscope (OM) and scanning electron microscope (SEM) were used to analyze the phase structure and microstructure of Fe-based alloy coatings, and the hardness and tribological properties were measured by the microhardness tester and ball on disc wear tester, respectively. The results show that the microstructure of conventional gravity feeding (GF) coatings was composed of coarse columnar crystals. In comparison, owing to the diversification of energy composition, the microstructure of the high-speed powder feeding (HF) coatings consists of uniform and small grains. The total energy of the HF process was 75.5% of that of the GF process, proving that high-efficiency cladding can be achieved at lower laser energy. The refinement of the microstructure is beneficial to improve the hardness and wear resistance of the coating, and the hardness of the HF coating increased by 9.4% and the wear loss decreased to 80.5%, compared with the GF coating. The wear surface of the HF coating suffered less damage, and the wear mechanism was slightly adhesive wear. In contrast, wear was more serious in the GF coating, and the wear mechanism was transformed into severe adhesive wear.

Keywords: laser cladding; high-speed powder feeding; Fe-based alloy; microstructure; wear resistance

check for updates

Citation: Wang, Q.; Qian, R.; Yang, J.; Niu, W.; Zhou, L.; Pan, X.; Su, C. Effect of High-Speed Powder Feeding on Microstructure and Tribological Properties of Fe-Based Coatings by Laser Cladding. *Coatings* **2021**, *11*, 1456. https://doi.org/10.3390/coatings11121456

Academic Editor: Damian Przestacki

Received: 26 October 2021
Accepted: 23 November 2021
Published: 26 November 2021

1. Introduction

Due to their high strength, good machining performance and low cost, steels are widely used in industrial fields of petroleum, coal, train and automotive manufacturing [1,2]. However, steels usually face a harsh working environment, which inevitably causes defects, such as scratches, cracks and corrosion pits on the surface, resulting in severe reduction of the equipment service life [3,4]. Therefore, the surface treatment of steels is necessary to improve their service performance [5,6].

As a surface protection technology, laser cladding uses laser energy to melt metallic powders on the surface of substrate to form a coating with metallurgical bonding [7–13]. However, owing to the formation of coatings completely relying on the input of laser energy, defects—such as cracks, holes and excessive heat-affected zone caused by excessive heat input or uneven energy density—often appear in the microstructure of coating [14–17]. For example, when repairing the defense-grade ultra-high strength steel by laser cladding,

the formation of non-tempered martensite adversely affected the mechanical properties of the part, and the subsequent heat treatment may also cause other harmful effects [18]. This greatly limits the application of laser cladding. Yan et al. [19] used laser cladding to prepare IN625 coatings on nickel-based superalloys (GTD-111) and studied the effect of powder feeding speed on the microstructure, defects and hardness of the coatings. The results revealed that as the powder feeding speed increased from 200 mg/s to 500 mg/s (in Table 1), the tendency to form equiaxed/coaxial regions in the coating zone decreased, and the distance between the dendritic arms at the bottom of the coating also decreased from 1.12 μm to 1.02 μm. The increase in powder feeding speed actually reduced the heat input of powder materials during laser cladding. Yi et al. [20] used synchronous powder-feeding underwater laser cladding to prepare a modified 434 ferritic stainless-steel coating on A32 deck steel. As the powder feeding rate increased from 175 mg/s to 263 mg/s (in Table 2), the coating structure was refined. Therefore, the powder feeding rate significantly affects the coating structure during laser cladding process.

Table 1. Laser cladding parameters [19].

Track	Pav (W)	V (mm/s)	F (mg/s)
MT1	150	5	300
MT2	200	5	300
MT3	250	5	300
MT4	300	5	300
MT5	200	4	300
MT6	200	6	300
MT7	200	7	300
MT8	200	5	200
MT9	200	5	400
MT10	200	5	500

Table 2. Laser cladding parameters [20].

Iron−Based	Powder−Feeding Gas Flow Rate (L/min)	Laser Power (W)	Powder−Feeding Rate (mg/s)
A	8	1200	175
B	8	2000	175
C	16	2000	175
D	16	2000	263
E	20	2000	263
F	22	2000	263
G	24	2000	263
H	26	2000	263
I	30	2000	263

During the process of laser cladding, powder materials are normally injected through a straight tube, where particles flow at a low speed. In order to motivate the effect of the powder feeding rate, in terms of the amount of powder materials and the speed of powder particles, the powder feeding system was modified in the present study, i.e., a convergent-divergent Laval nozzle structure was used in replacing the cylindrical tube to accelerate powder particles to a high speed during the laser cladding process. The influence of high-speed powder feeding on the microstructure, phase composition, microhardness and wear resistance of laser cladded coatings on the surface of 27SiMn steel substrate is comprehensively discussed.

2. Experiment

27SiMn steel (100 × 50 × 10 mm) was used as the substrate, and its chemical composition is listed in Table 3. Prior to the laser cladding, the substrate was grinded and ultrasonically cleaned with ethanol to remove stains from the surface. The gas atomized

Fe-based alloy powder was used as source material for laser cladding, and the chemical composition is shown in Table 4. The powder morphology in Figure 1a shows a spherical shape, and the average particle size shown in Figure 1b is 100 μm, measured by a laser particle size distribution analyzer (LS-809, Dandong Better Instruments Co., Ltd., Dandong, China). Before the experiment, powders were dried in a vacuum furnace at 80 °C for 3 h.

Table 3. Chemical composition of 27SiMn steel (wt%).

C	Si	Mn	P	S	Cr	Ni	Cu	Mo	Fe
0.24–0.32	1.1–1.4	1.1–1.4	≤0.035	≤0.035	≤0.3	≤0.3	≤0.3	≤0.15	bal

Table 4. Chemical composition of Fe-based alloy powder (wt%).

C	Cr	Ca	Ni	Mo	Co	Fe
0.15	18.79	1.85	13.92	3.41	3.13	bal

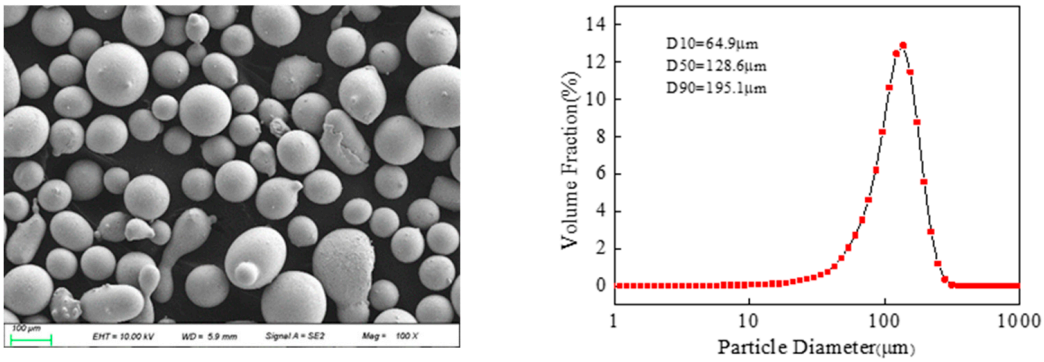

(**a**) (**b**)

Figure 1. (**a**) SEM morphology of Fe-based alloy powder; (**b**) the diameter distribution of Fe-based powder alloy particle.

As shown in Figure 2a, the laser cladding equipment (Shaanxi Tianyuan-LCD, Shaanxi Tianyuan Intelligent Remanufacturing Co., Ltd., Xi'an, China) was used to prepare the coatings, and high-purity N_2 and Ar was used as the working and shielding gas, respectively. Fe-based alloy powder was feed through the coaxial gravity feeding (marked as GF) with straight nozzle, and Table 5 lists the process parameters. As shown in Figure 2b, the high-speed powder feeding (marked as HF) system (Xi'an University of Architecture and Technology, Light Alloy Rapid Additive Manufacturing Technology R&D Center, Xi'an, China) was mainly composed of a high-pressure chamber and convergent-divergent Laval nozzles instead of straight ones. The working gas through the high-pressure chamber was N_2, and the gas preheating temperature and gas pressure was set at 300 °C and 8 bar, respectively. During the laser cladding process, the deposition temperature was measured in real time by infrared thermometer. The motion control system was a 6-axis vertical articulated robot (Motoman-AR1440, Yaskawa Electric Corporation, Shanghai, China), with a control accuracy of 0.01 mm. Table 6 lists the process parameters of the HF process.

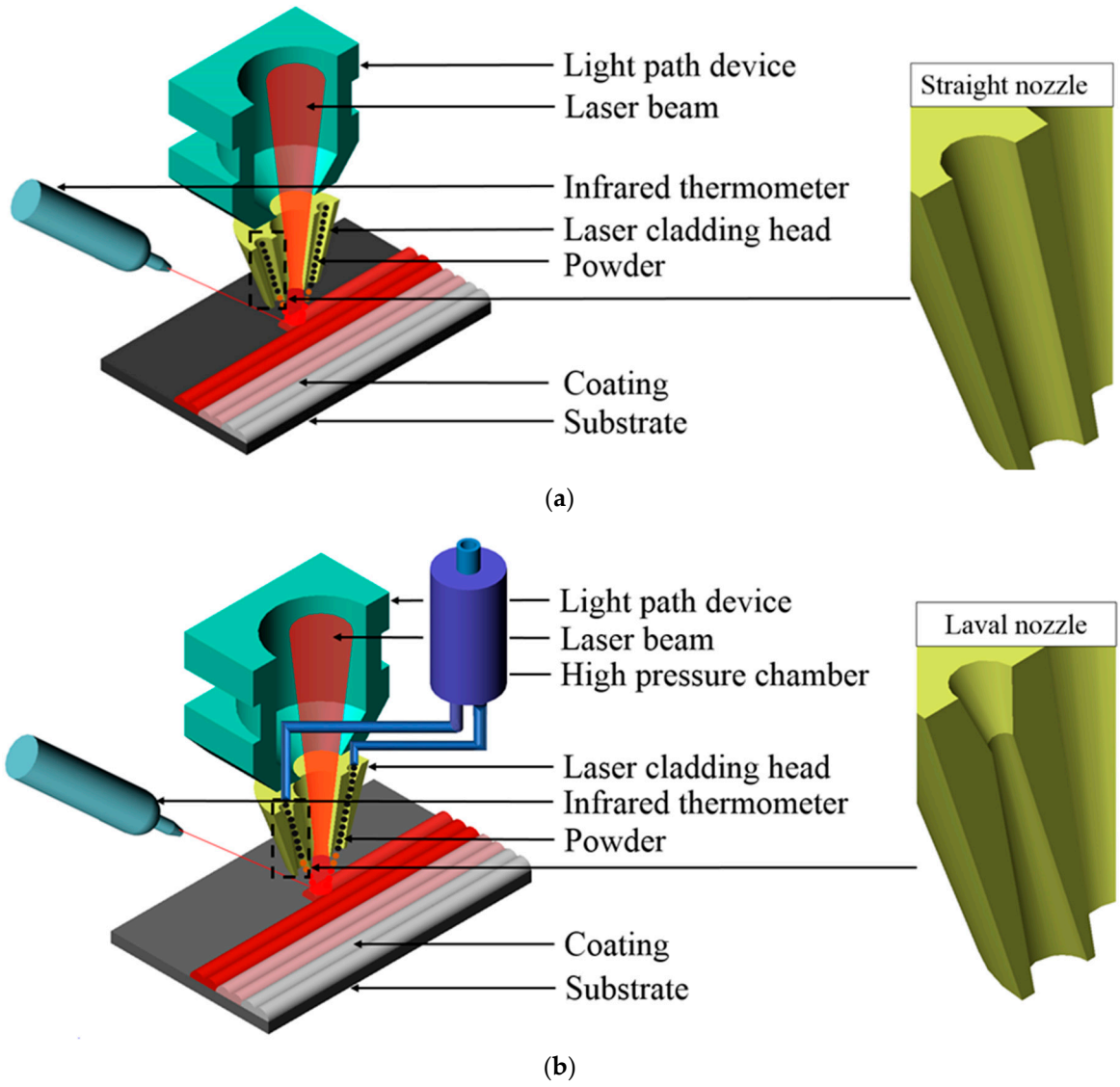

Figure 2. Schematic diagram: (**a**) GF process; (**b**) HF process.

Table 5. Process parameters of GF.

Feeding Rate (g/min)	Scanning Velocity (mm/s)	Work Distance (mm)	Working Gas	Shielding Gas	Laser Power (kW)
25	5	15	N_2	Ar	2.0

Table 6. Process parameters of HF.

Work Distance (mm)	Scanning Speed (mm/s)	Feeding Rate (g/min)	Laser Power (kW)
15	15	60	1.6

After laser cladding, samples were cut into a size of 5 × 5 × 3 mm, and polishing and grinding were done for microstructure observation, by using a field emission scanning electron microscope (SEM, Gemini SEM 300, Carl Zeiss AG, Jena, Germany) and Optical microscope (OM, Sunny Optical Technology Co., Ltd., Yuyao, China). The phase composition of the coatings and powder was analyzed by X-ray diffractometer (D8 ADVANCE,

Bruker, Billerica, MA, USA). The copper target (Cu-Kα, λ = 0.154056 nm) was used, and the operating parameters are voltage 40 kV, current 40 mA, measuring range 10–80° and scanning speed 5 °/min. The microhardness of coatings and substrate was measured by Vicker's hardness test, under 0.3 kg load for 20 s.

The MS-T3001 ball-disk friction and wear tester (Jinan Jingcheng Testing Technology Co., Ltd., Jinan, China) was used to conduct friction and wear experiments on the 27SiMn steel substrate and coatings, and the schematic diagram of the friction and wear process is shown in Figure 3. Before experiment, grinding and polishing of the sample were conducted, followed by cleaning with alcohol solution in ultrasonic cleaning machine (GS50-200, Guangdong Good Ultrasound Co., Ltd., Meizhou, China) for 60 min. The surface roughness was measured as 10 μm. The size of sample for wear is 10 × 10 × 5 mm. The sample was clamped at the center by the baffle, and the grinding ball was located on the surface of the coating or substrate. Through long-term rotation, the grinding ball will form a ring-shaped wear trace on the surface of the coating or substrate. The results were averaged based on three tests for each sample. GCr15 ball with a diameter of 6 mm was used as the friction pair, and the wear radius 3 mm, the normal load 20 N, the disc rotating speed 200 r/min and the time 30 min were used. Optical instrument (RTEC UP-Lambda, Pomeas Technology Co., Ltd., Dongguan, China) was used to measure volumetric wear, and the average volume wear of three samples were calculated.

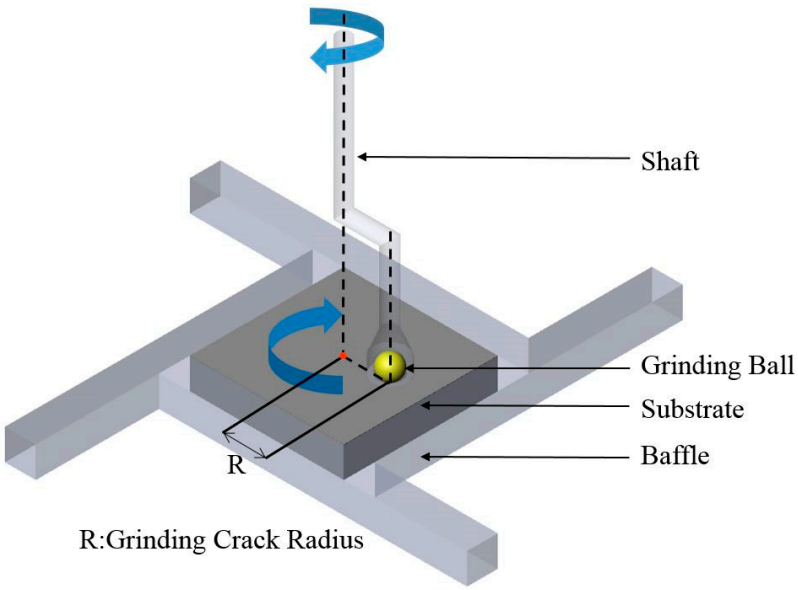

Figure 3. Schematic diagram of friction and wear experiment.

3. Results and discussion

3.1. Microstructure

Figure 4 shows the cross-sectional microstructure of coating/substrate interface under different processes, and the heat-affected zone (HAZ) was labeled. The wave shape appears at the interface between the coating and the substrate, which is caused by the gradual decrease of the laser energy density distribution from the center to the periphery. Therefore, the bottom boundary of the heat affected zone also presents a shallow wave shape [21]. After five measurements for each sample, the average thickness of the coating and HAZ is obtained, and the thickness results are shown in Figure 5. It can also be seen that the thickness of the HF coating (446 μm) is smaller, compared with the GF coating (615 μm). During the process of HF, some larger particles rebounded during high-speed particle impact, resulting in a lower coating thickness [22]. According to the thickness of HAZ in Figure 4, it can be seen that HAZ of GF (502 μm) is greater than that of HF (317 μm). The reason for this phenomenon is that the heat input of the GF process is 1.3 times that of the HF process, resulting in more heat absorbed by the substrate [23].

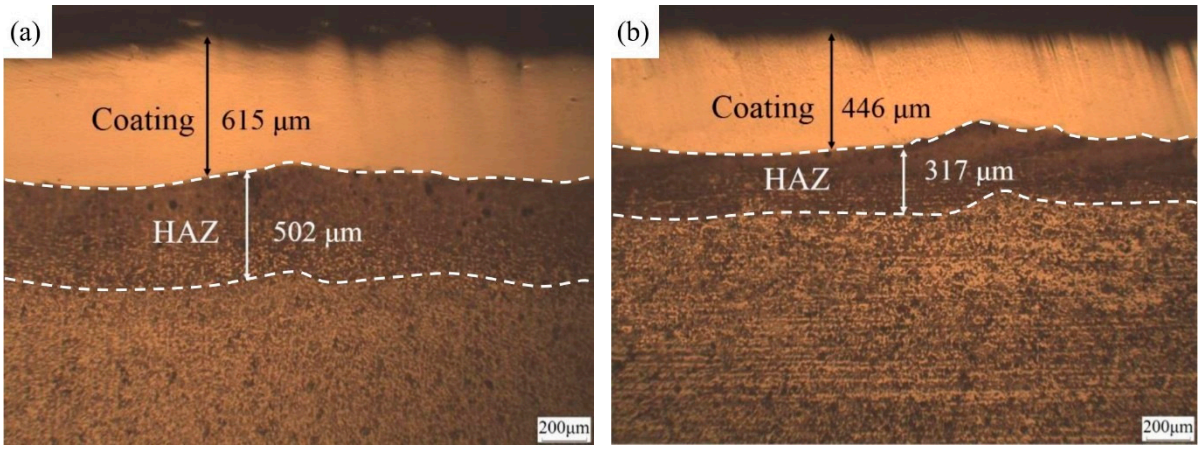

Figure 4. The cross-sectional microstructure of coating: (**a**) GF; (**b**) HF.

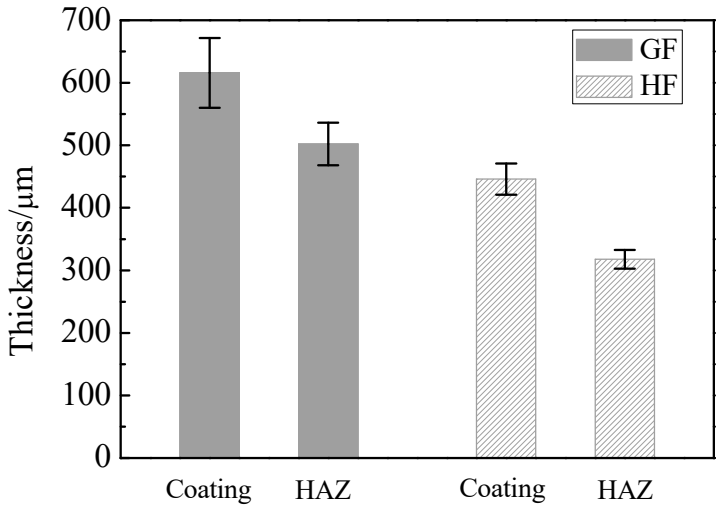

Figure 5. Thickness of coating and HAZ.

Figure 6a,c,e shows the cross-sectional microstructure of the bottom, middle and top of the coating under the GF process. It can be seen that different regions correspond to different morphologies. Since a high energy density laser beam is introduced in the GF process, the purpose of rapid heating and rapid solidification can be achieved in the process of preparing the coating, so the GF solidification structure grows from the bottom of the molten pool to the top. Meanwhile, the solidification characteristics of the GF coatings strongly depends on the value of G/R (G represents the temperature gradient; R represents the solidification rate). According to Figure 7, it can be seen that different G/R values correspond to different morphologies of solidified structures [20,24]. The value of G/R is larger at the bottom of the molten pool, and the crystal growth rate at this time is much greater than the nucleation rate, so the grains grow into coarse columnar crystals [25]. For the top of the coating, due to the smaller G and the larger R, the growth rate of grains is lower than the nucleation rate. Therefore, the grains mainly grow into small columnar crystals, and they tend to grow in a certain direction [26]. Figure 6b,d,f shows the cross-sectional microstructure of the bottom, middle and top of the HF coating. The HF coating exhibits a completely different morphology from the GF coating, and no columnar crystals were found, mainly composed of fine grains.

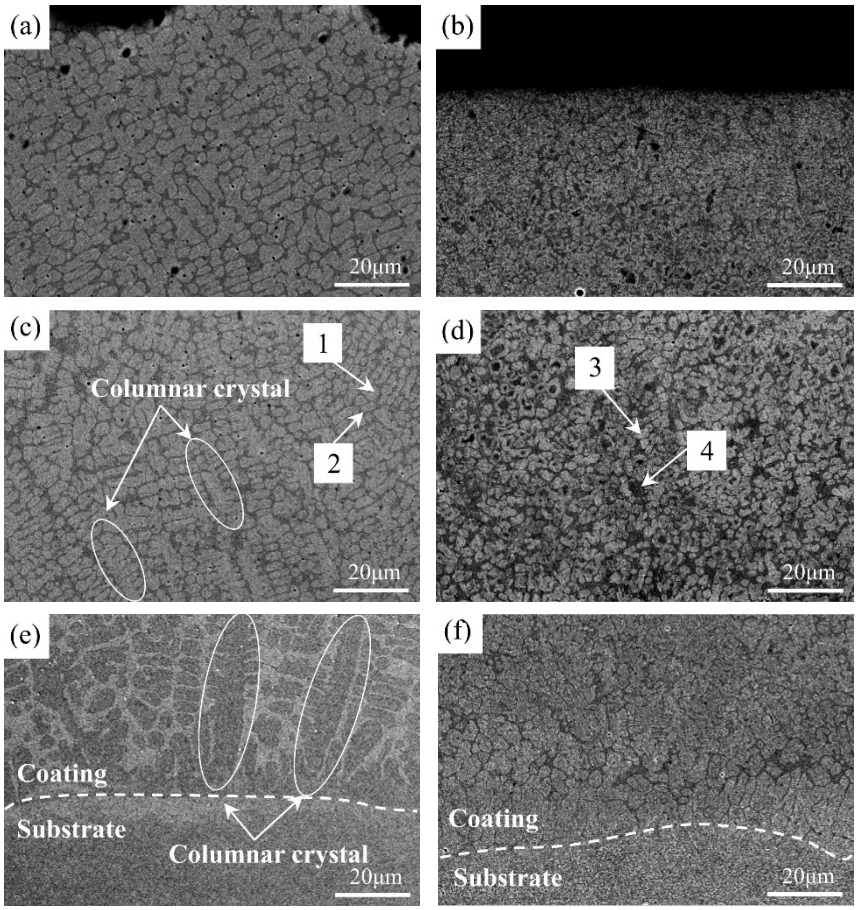

Figure 6. Microstructure of coating: (**a**) top of the GF coating; (**b**) top of the HF coating; (**c**) middle of the GF coating; (**d**) middle of the HF coating; (**e**) bottom of the GF coating; (**f**) bottom of the HF coating.

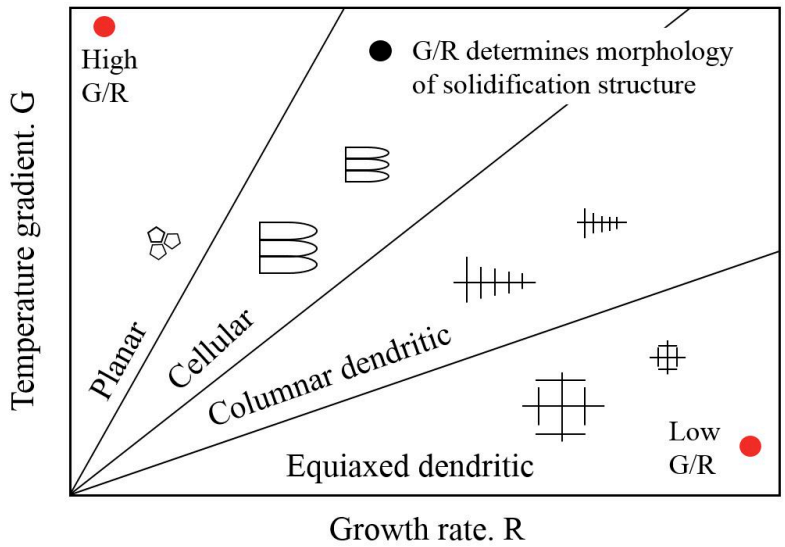

Figure 7. The relationship between G and R and their effect on morphology of solidification structure [20].

In the HF process, the total energy of high-speed particles deposited on the substrate material (or deposited coating) is composed of the particle's own energy (including kinetic energy and thermal energy) and the thermal energy generated by the laser. In the GF

process, the powder is fed by gravity and the powder is not preheated, so the total energy of the laser cladding process is only the thermal energy generated by the laser [27]. The formula mentioned above is as follows:

$$E = E_k + E_{th} \tag{1}$$

$$E_k = \frac{1}{2} m V_P^2 \tag{2}$$

$$E_{th} = c_p \left(T_p - T_{ref} \right) \tag{3}$$

$$GF : E = E_{th}(laser) \tag{4}$$

$$HF : E = E_k(powder) + E_{th}(powder) + E_{th}(laser) \tag{5}$$

where E is the total energy; E_k is the kinetic energy; E_{th} is the thermal energy; V_p is the impact velocity of the particles; c_p is the initial temperature when the particles collide; T_{m} is the melting point of the particles; and T_{ref} is the reference temperature (usually room temperature). The total energy of the GF and HF process correspond to Formula (4) and (5) respectively. Table 7 shows the calculation results of the GF processes. It can be seen that because only the laser energy is introduced in the GF process, the total energy of the GF process is the heat generated by the laser. The difference from the GF process is that the powder of the HF process has a certain amount of thermal energy and kinetic energy before it comes into contact with the laser. As can be seen from Table 8, the total energy of the HF process consists of the thermal energy provided by the laser, the thermal energy of the powder undergoing preheating and the kinetic energy of the powder running at a high speed. Numerical simulation was carried out by using fluid mechanics software (ANSYS-Fluent), based on the mode of gas–solid dynamics [28]. The powder feeding airflow was N_2, the powder material was Fe-based alloy powder, the powder particle size was 100 μm and the air inlet temperature and pressure were set to 573 K and 8 bar, respectively. Figure 8 shows the calculated particle velocity distribution diagram. It is noted that although the HF process introduces the kinetic energy of the particles, the kinetic energy of the particles is extremely small compared to the thermal energy due to the low weight of the powder particles. Therefore, the total energy of the HF process is almost all of the thermal energy (E_{th}(powder)+E_{th}(laser)). During the HF process, laser thermal energy accounts for 80.9% of the total energy, and powder thermal energy accounts for 19.1% of the total energy. According to the data in Tables 7 and 8, it can be seen that the total energy of the HF process is lower, which is 75.5% of the total energy of the GF process. Due to the diversified energy input of the HF process, the powder with a certain amount of energy is conducive to the formation of a finer microstructure during deposition. Meanwhile, due to the reduction of laser energy, excessive heat-affected zone (HAZ) caused by excessive heat input can be avoided.

Table 7. Energy calculation of the GF process.

c_p (J/°C)	T_p (°C)	T_{ref} (°C)	M (kg)	V_p (m/s)	E_k (J)	E_{th} (J)	E (J)
0.46×10^3	1950	20	-	-	-	8.87×10^5	8.87×10^5

Table 8. Energy calculation of the HF process.

		c_p (J/°C)	T_p (°C)	T_{ref} (°C)	m (kg)	V_p (m/s)	E_k (J)	E_{th} (J)	E (J)
Energy of laser (E_{th})		0.46×10^3	1480	300	-	-	-	5.42×10^5	6.70×10^5
Energy of powder	Thermal energy (E_{th})	0.46×10^3	300	20	-	-	-	1.28×10^5	
	Kinetic energy (E_k)	-	-	-	1×10^{-3}	397	78	-	

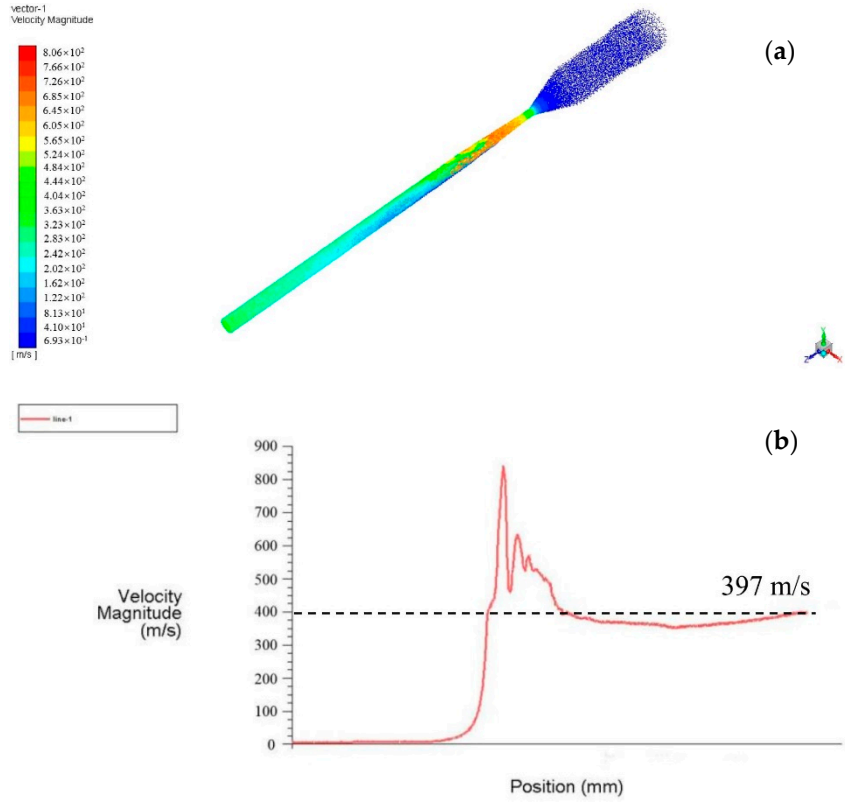

Figure 8. (**a**) The velocity distribution diagram of powder particles in the Laval tube; (**b**) the velocity–position curve of the powder particles in the Laval tube.

3.2. Phase Analysis

In order to explore the influence of diversified energy composition on the phases of laser cladding coatings, phase and EDS analysis of the original powder, GF and HF coatings were carried out, and the corresponding XRD patterns are shown in Figure 9. Based on the XRD pattern, and the EDS data in Table 9, Ni-Cr-Co-Mo, Fe-Cr, γ-Fe and (Fe, Ni) are the main phases in the HF coating, and the Fe-Cr and (Fe, Ni) are the main strengthening phases of Fe-based alloy [29]. As can be seen from Figure 9b,c, the difference in the phase of XRD pattern between the GF and the HF coating is that the GF coating generated a new phase $CaNi_3C_{0.5}$. According to the EDS results reported in Table 9, Points 1 and 2 contain higher Ni, C and Ca contents and lower Fe, Co and Cr contents comparing with points 3 and 4, as marked in Figure 6c,d. Due to the higher heat input and dilution effect of the GF process, the excess carbon and calcium on the surface of the coating and the substrate diffuse rapidly to form $CaNi_3C_{0.5}$ with Ni. Therefore, the elements in $CaNi_3C_{0.5}$ may not all come from the coating, and some elements may come from the substrate. It is noted that the phases in the HF coating are similar to those of the Fe-based powder, and this also confirms that the lower heat input can maintain the original powder phase [30]. When the process of coating preparation is changed, the peak shifts to a lower diffraction angle, indicating that the residual stress in the sample is increased [31]. This residual stress is usually caused by the rapid heating and rapid cooling during the laser cladding process. As revealed in Figure 9d, the diffraction peaks of the Fe-Cr phase under the HF process gradually broaden and the intensity decreases, which means that the Fe-Cr phase prepared by the HF process in this case forms a fine crystal and microstructure [32,33].

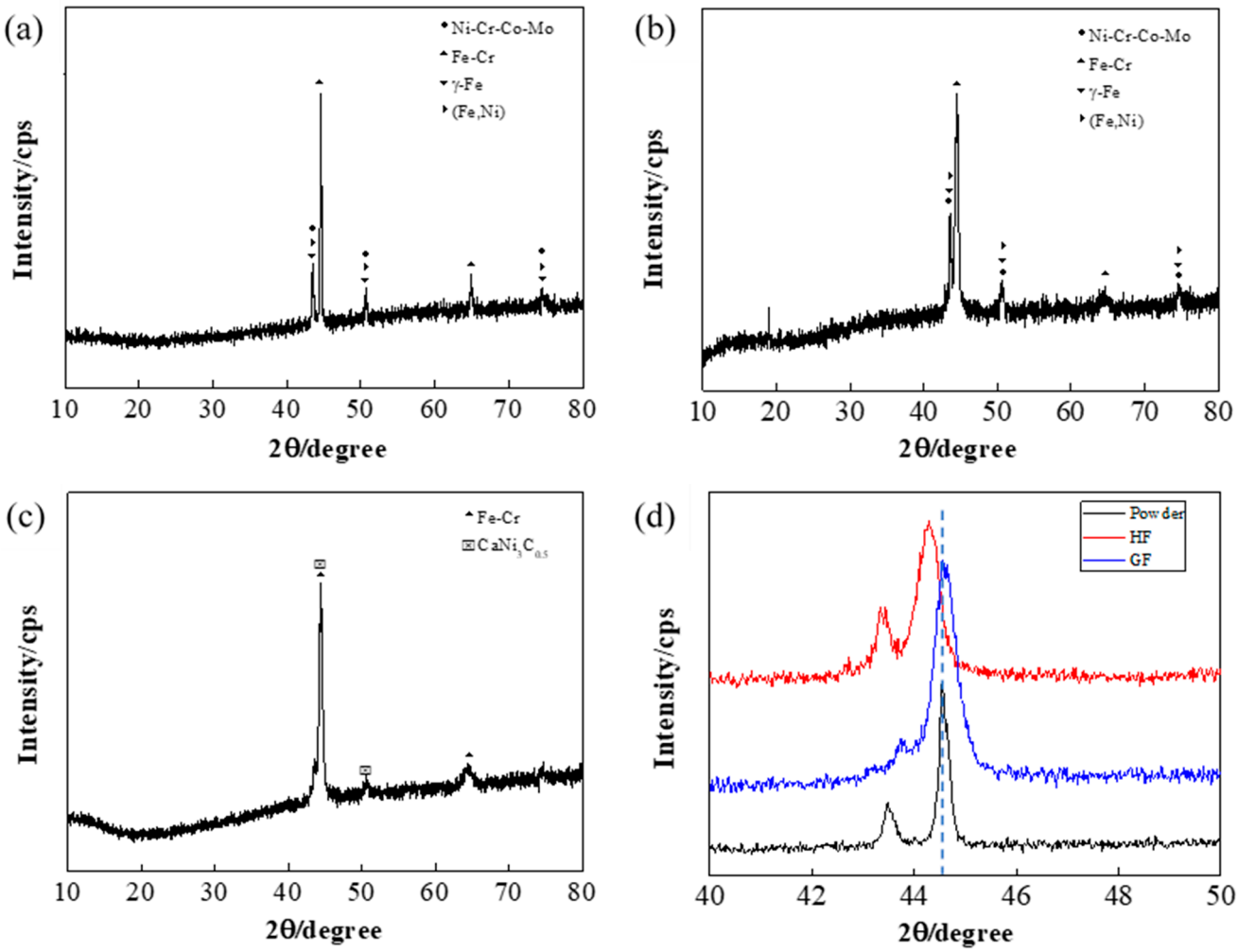

Figure 9. The XRD diffraction pattern of Fe-based powder and coatings: (**a**) Fe-based alloy powder; (**b**) HF coating; (**c**) GF coating; (**d**) comparison of the peak position of Fe-Cr phase in original powder and coatings.

Table 9. Elemental concentrations (wt.%) of the selected areas in the GF and HF coatings from EDS analysis.

	Fe	Cr	Ni	C	Co	Mo	Ca	O
Point 1	59.3	13.9	13.2	5.7	2.2	2.1	2.1	1.5
Point 2	57.7	11.5	16.7	7.1	3.1	-	1.9	2.0
Point 3	60.1	15.4	7.5	3.2	6.2	5.1	0.7	1.8
Point 4	63.2	14.7	6.8	2.1	6.5	4.3	0.1	2.3

3.3. Microhardness Analysis

Figure 10 shows the microhardness distribution curve of the HF and GF coatings along the depth of the layer. It can be observed that the microhardness distribution of the HF and GF coating presents three areas, which are the coating, the HAZ and the substrate. The result shows that the average microhardness of 27SiMn steel substrate is 175 HV0.3. The average microhardness of the HF coating is 604 HV0.3 and is 9.4% higher than that of the GF coating (543 HV0.3). Because the substrate absorbs part of the heat generated by the laser during the laser cladding, a transition zone (HAZ) is generated at the lower part of the interface, and the microhardness of HAZ will gradually decrease and approach the substrate. During the HF process, due to the impact of the high-speed running powder, the microstructure of the coating changes from coarse columnar crystals to fine grains. In addition, the HF process has a faster scanning speed, which increases the cooling rate of

the coating during solidification. The fast cooling rate is beneficial to the formation of uniform and fine microstructure during the cladding process, which also improves the microhardness of the coating [34].

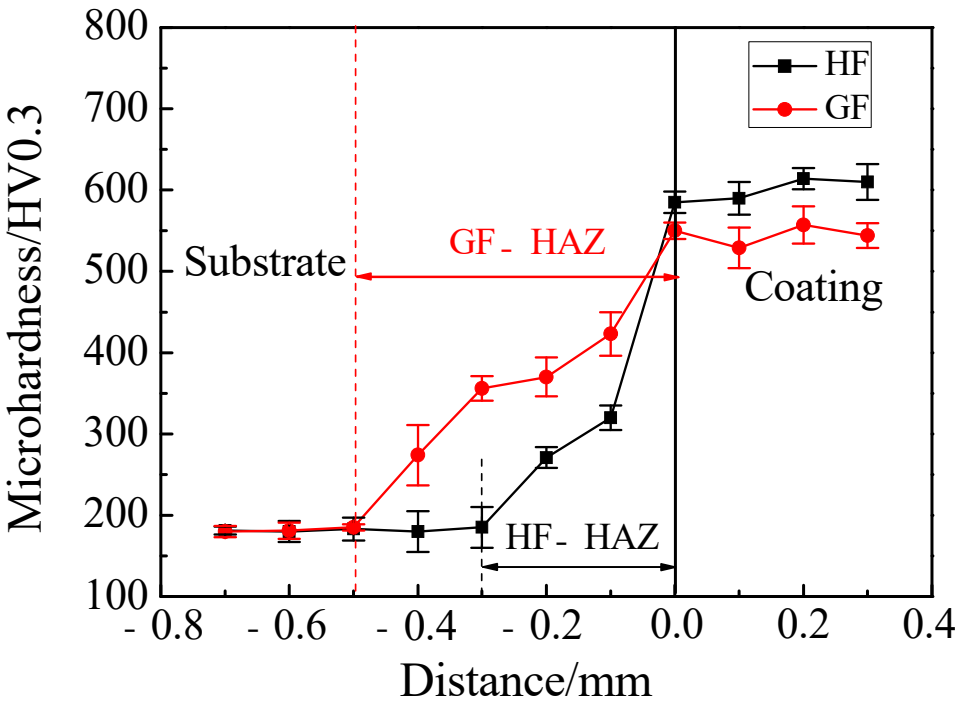

Figure 10. Microhardness curves of the GF and HF coating.

3.4. Tribological Performance Analysis of Coating and Substrate

Based on certain experimental parameters, friction and wear tests were carried out on the 27SiMn steel substrate, the GF coating and the HF coating. The relationship between friction coefficient (COF) and time of the substrate, GF coating and HF coating is compared. The curve of COF with time is shown in Figure 11. It can be seen that the COF curve of the 27SiMn steel substrate and the coatings can be divided into the initial wear stage and the stable wear stage. In the initial wear stage, the friction coefficient of 27SiMn steel slowly decreases from 0.75 to 0.45. According to Figure 12, it can be seen that the contact area between the GCr15 grinding ball and the surface of the 27SiMn steel is relatively small. Owing to the hardness of the GCr15 grinding ball being higher than that of the 27SiMn steel, when the grinding ball acts on the substrate, the local stress is higher than the yield limit of the substrate material, resulting in greater pressing depth and resistance f. The COF of the 27SiMn steel substrate at the initial wear stage gradually decreased from 0.75 to 0.45. Due to the GCr15 grinding ball in the initial wear stage having a higher hardness and a smaller contact area with the surface of the substrate, the local stress generated at this time is higher than the yield limit of the substrate, which causes the grinding ball's pressing depth and resistance f to be larger. Meanwhile, owing to the friction pair needing to overcome the adhesion force $\sigma_f \cdot S$ (σ_f is the shear stress of the 27SiMn steel substrate, and S is the area of the bonding area) during the movement process, the COF of the 27SiMn steel substrate at the initial wear stage is relatively large. Under the cyclic movement, the material in the friction pair area gradually hardened, and the pressing depth of the GCr15 ball and the area of the adhesion area gradually decreased, so the COF decreased and gradually entered the stable wear stage.

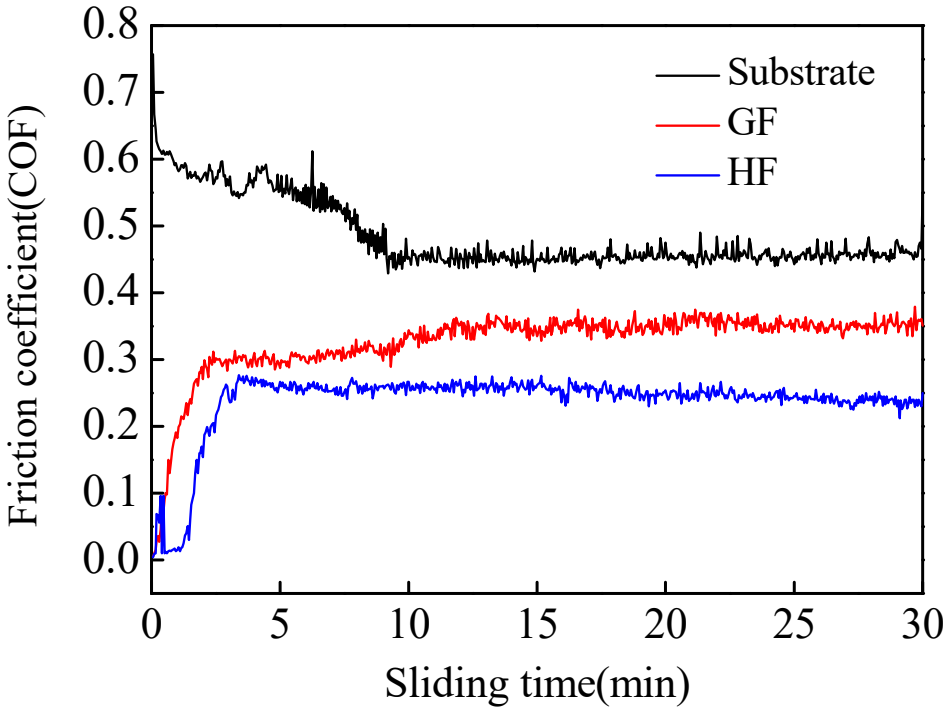

Figure 11. The friction coefficient curve of the substrate, GF and HF coating.

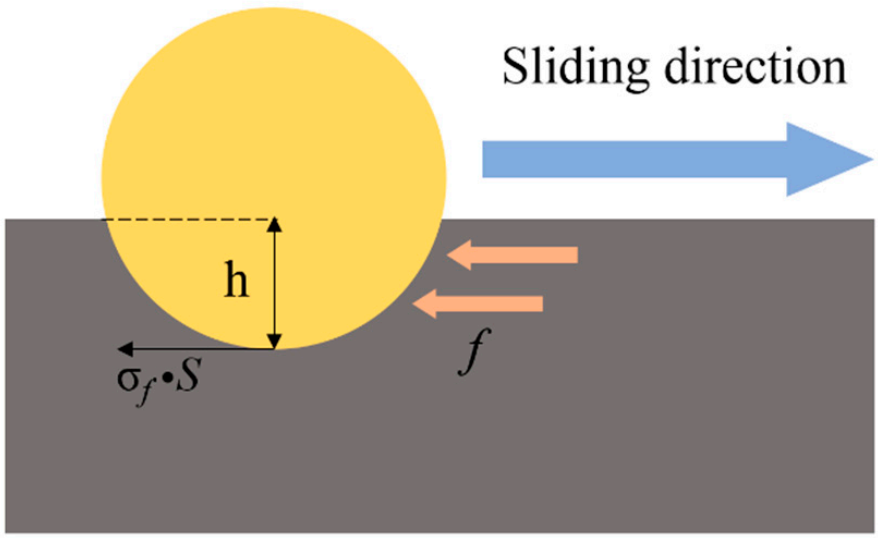

Figure 12. Forces on the GCr15 ball and substrate during the friction and wear experiment.

In comparison, the wear curves of the HF and GF coatings and the 27SiMn steel substrate are quite different. In the initial stage of wear, the friction coefficients rapidly increase from 0 to 0.27 and 0.30, respectively. The coating with higher hardness makes the pressing depth of the grinding ball shallow, resulting in less resistance f to the grinding ball during the friction stage. Through the cyclic wear of the grinding ball on the surface of the substrate, the contact area between the grinding ball and the surface of the substrate gradually becomes smooth, so the friction coefficient gradually increases. Finally, the COF of the HF and GF coatings stabilized at around 0.23 and 0.37, respectively. Due to the surface peeling and wear of the coating during the friction process, the COF will fluctuate, but the friction curve of the HF coating is the most stable. The wear volume of the 27SiMn steel substrate, the HF and GF coatings is shown in Figure 13. It can be noted that the HF coating has the lowest wear volume. The wear volume of the HF coating and the GF

coating are 21.9% and 27.2% of the 27SiMn steel substrate, respectively, indicating that the wear resistance of the HF coating was better than that of the traditional GF coating. In the study of Kalyanasundaram et al. [35], they deposited diamond on the aluminum alloy substrate by electrodeposition technology. After conducting nanoindentation and wear experiments, they found that as the microhardness increases, the friction coefficient of the coating reduces from 0.60 to 0.32. Experience has proved that the microhardness of the coating is the main factor that determines the wear resistance, and the increase of the microhardness of the coating will increase the wear resistance.

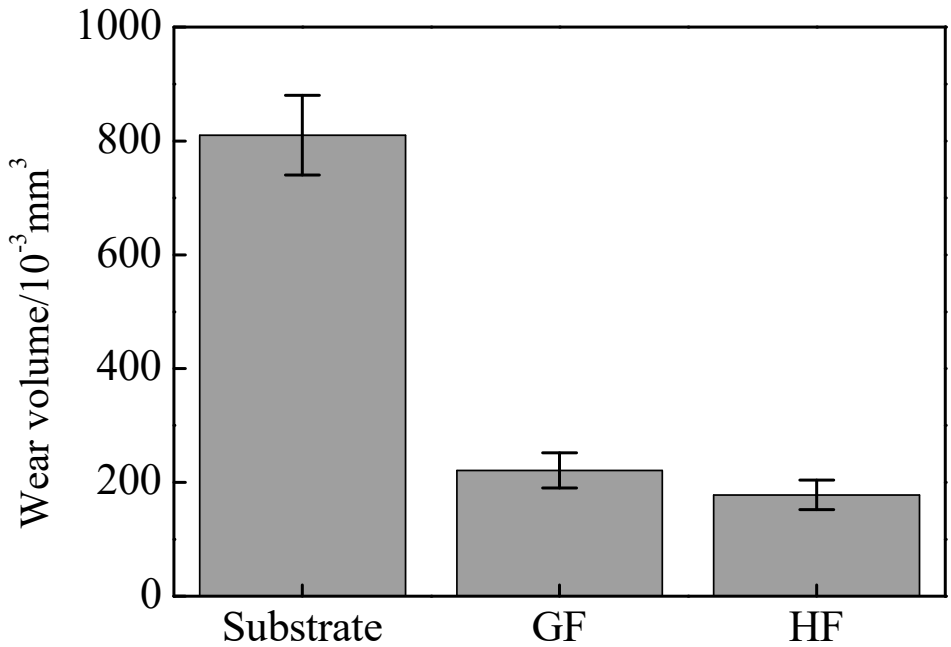

Figure 13. Volume loss of substrate, GF and HF coating.

Figure 14 shows the wear morphology of the coating and substrate surface. It can be seen from Figure 14a,b that there are obvious grooves and adhesive peeling on the surface of 27SiMn steel, which indicates that abrasive wear and adhesive wear have occurred during the wear process. Due to the harder grinding balls being pressed into the 27SiMn steel to a certain depth, adhesion is formed on the surface of the substrate. The material on the surface of the substrate peels off after undergoing plastic deformation, and the smaller abrasive debris plow the surface and form furrows. With the cyclic movement of the grinding ball, a large area of peeling occurs on the surface of the substrate, so the wear loss of the 27SiMn steel substrate is relatively large.

Figure 14c,d shows the wear morphology of the GF coating. It can be seen that there is obvious adhesion in the middle of the wear track, and a large number of cracks and lamellar spalling appear on both sides of the wear track, which indicates that the wear mechanism of the GF coating is severe adhesive wear. Figure 14e,f shows the wear morphology of the HF coating. When the powder undergoes acceleration and preheating in the HF process, the wear resistance of the prepared coating is improved, and no obvious cracks and large-area peeling are found. Compared with the GF coating, the HF coating surface experiences less damage, and the worn grooves are narrow and shallow. Therefore, the wear mechanism of the HF coating is dominated by slight adhesive wear. From the previous tribological analysis, it can be seen that the uniform and fine structure is beneficial to improve the wear resistance of the coating, and effectively reduces the ploughing effect of the grinding ball on the surface of the material [36–38].

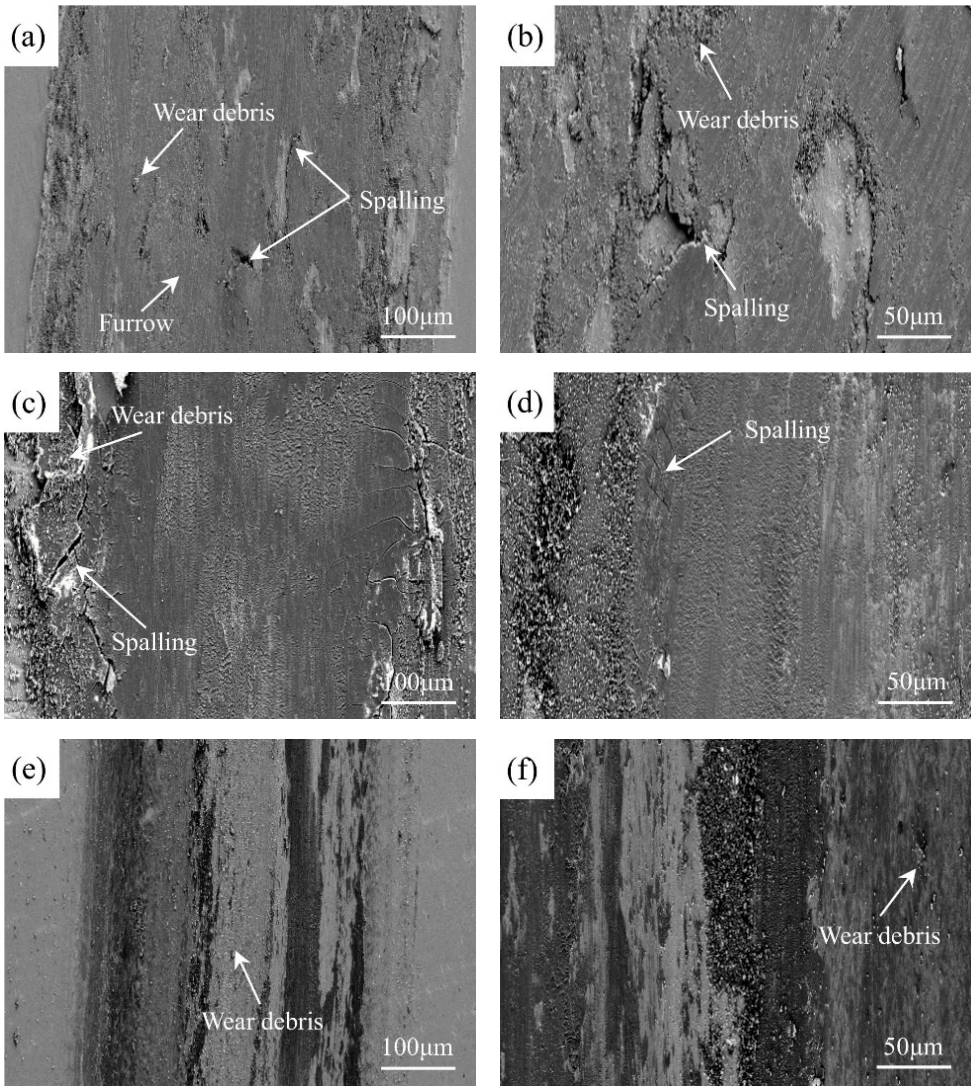

Figure 14. Wear trajectory topography: (**a**,**b**) substrate; (**c**,**d**) GF coating; (**e**,**f**) HF coating.

4. Conclusions

(1) In order to motivate the effect of powder feeding rate, in terms of the amount of powder materials and the speed of powder particles, the powder feeding system was modified in the present study, i.e., a convergent–divergent Laval nozzle structure was used in replacing the cylindrical tube to accelerate powder particles to a high speed during laser cladding process. The main findings are as follows:

(2) The microstructure of GF coatings is mainly composed of coarse columnar crystals, in which the columnar crystals have obvious growth direction. Owing to the diversification of energy composition in the HF process, the microstructure of HF coatings changes from coarse columnar crystals to uniform and small grains. The total energy of the HF process is 75.5% of that of the GF process, which can achieve high-efficiency cladding at low energy.

(3) The hardness of the laser cladding coating prepared by the GF and HF process is higher than that of the 27SiMn steel substrate. As the HF coating has a finer microstructure, this will help improve the hardness of the coating. The maximum microhardness of the HF coating is 604HV0.3, which is 9.4% higher than that of the GF coating.

(4) The HF coating prepared by laser cladding on the surface of the 27SiMn steel substrate can effectively protect the substrate material, and the higher hardness makes the HF coating have better wear resistance. Compared with the GF coating, the COF of the HF coating is reduced to 0.23, the wear volume is reduced by 19.5% and the wear mechanism is changed to slight adhesive wear.

Author Contributions: Q.W.: Conceptualization, Formal analysis, Writing—review and editing. R.Q.: Investigation, Writing—original draft preparation. J.Y.: Investigation, Formal analysis. W.N.: Methodology, Conceptualization. L.Z.: Validation, Formal analysis, Resources, Data curation. X.P.: Validation, Formal analysis, Resources. C.S.: Validation, Formal analysis, Resources. All authors have read and agreed to the published version of the manuscript.

Funding: This work was supported by the Natural Science Foundation of China (Grant No. 51801143), the Natural Science Foundation of Shaanxi Province (Grant No. 2017JZ012), and the Education Department of Shaanxi Province (Grant No. 18JK0445).

Institutional Review Board Statement: Not applicable.

Informed Consent Statement: Not applicable.

Data Availability Statement: Not applicable.

Conflicts of Interest: The authors declare no conflict of interest.

References

1. Collard-Wexler, A.; De Loecker, J. Reallocation and Technology: Evidence from the U.S. Steel Industry. *Am. Econ. Rev.* **2013**, *105*, 131–171. [CrossRef]
2. Zhang, H.; Hong, X. An overview for the utilization of wastes from stainless steel industries. *Resour. Conserv. Recycl.* **2011**, *55*, 745–754.
3. Alexeev, A.A.; Bolshev, K.N.; Ivanov, V.A.; Syromyatnikova, A.S.; Kovalenko, A.N. Experimental determination of crack velocities in steel. *Procedia Struct. Integr.* **2020**, *30*, 1–5. [CrossRef]
4. Tiberti, G.; Trabucchi, I.; AlHamaydeh, M.; Minelli, F.; Plizzari, G.A. Crack development in steel-fibre-reinforced concrete members with conventional rebars. *Mag. Concr. Res.* **2019**, *71*, 599–610. [CrossRef]
5. Yang, Y.W.; Fu, H.G.; Ju, J.; Lei, Y.P.; Zhu, L.L.; Jiang, L. Phase diagram caGFulation and analyze on cast high vanadium wear-resistant alloy. *Metall. Res. Technol.* **2017**, *114*, 314. [CrossRef]
6. Gong, J.; Zhang, D.; Liu, C.; Zhao, Y.; Hu, P.; Quan, W. Optimization of electro-hydraulic energy-savings in mobile machinery. *Autom. Constr.* **2019**, *98*, 132–145. [CrossRef]
7. Wang, D.; Tian, Z.; Wang, S.; Shen, L.; Liu, Z. Microstructural characterization of Al_2O_3–13 wt.% TiO_2 ceramic coatings prepared by squash presetting laser cladding on GH4169 superalloy. *Surf. Coat. Technol.* **2014**, *254*, 195–201. [CrossRef]
8. Baldridge, T.; Poling, G.; Foroozmehr, E.; Kovacevic, R.; Metz, T.; Kadekar, V.; Gupta, M.C. Laser cladding of Inconel 690 on Inconel 600 superalloy for corrosion protection in nuclear applications. *Opt. Lasers Eng.* **2013**, *51*, 180–184. [CrossRef]
9. Wang, K.; Du, D.; Liu, G.; Chang, B.; Ju, J.; Sun, S.; Fu, H. Microstructure and property of laser clad Fe-based composite layer containing Nb and B4C powders. *J. Alloys Compd.* **2019**, *802*, 373–384. [CrossRef]
10. Lei, J.; Shi, C.; Zhou, S.; Gu, Z.; Zhang, L.C. Enhanced corrosion and wear resistance properties of carbon fiber reinforced Ni-based composite coating by laser cladding. *Surf. Coat. Technol.* **2018**, *334*, 274–285. [CrossRef]
11. Luo, X.; Yao, Z.; Zhang, P.; Gu, D.; Chen, Y. Laser Cladding Fe-Al-Cr Coating with Enhanced Mechanical Properties. *J. Wuhan Univ. Technol.-Mater. Sci. Ed.* **2019**, *34*, 1197–1204. [CrossRef]
12. Tian, J.; Xu, P.; Chen, J.; Liu, Q. Microstructure and phase transformation behaviour of a Fe/Mn/Si/Cr/Ni alloy coating by laser cladding. *Opt. Lasers Eng.* **2019**, *122*, 97–104. [CrossRef]
13. Rahman Rashid, R.A.; Javed, M.A.; Barr, C.; Palanisamy, S.; Matthews, N.; Dargusch, M.S. Effect of in situ tempering on the mechanical, microstructural and corrosion properties of 316L stainless steel laser-cladded coating on mild steel. *Int. J. Adv. Manuf. Technol.* **2021**, *117*, 2949–2958. [CrossRef]
14. Fesharaki, M.N.; Shoja-Razavi, R.; Mansouri, H.A.; Jamali, H. Microstructure investigation of Inconel 625 coating obtained by laser cladding and TIG cladding methods. *Surf. Coat. Technol.* **2018**, *353*, 25–31. [CrossRef]
15. Yang, S.; Phung, T.A. Microstructure and properties of Cu/TiB_2 wear resistance composite coating on H13 steel prepared by in-situ laser cladding. *Opt. Laser Technol.* **2018**, *108*, 480–486.
16. Li, Y.; Dong, S.; Yan, S.; Li, E.; Liu, X.; He, P.; Xu, B. Deep pit repairing of nodular cast iron by laser cladding NiCu/Fe-36Ni low-expansion composite alloy. *Mater. Charact.* **2019**, *151*, 273–279. [CrossRef]
17. Zhu, Y.; Yang, Y.; Mu, X.; Wang, W.; Yao, Z.; Yang, H. Study on wear and RCF performance of repaired damage railway wheels: Assessing laser cladding to repair local defects on wheels. *Wear* **2019**, *430–431*, 126–136. [CrossRef]
18. Rashid, R.R.; Nazari, K.A.; Barr, C.; Palanisamy, S.; Orchowski, N.; Matthews, N.; Dargusch, M.S. Effect of laser reheat post-treatment on the microstructural characteristics of laser-cladded ultra-high strength steel. *Surf. Coat. Technol.* **2019**, *372*, 93–102. [CrossRef]
19. Cao, Y.; Farouk, N.; Taheri, M.; Yumashev, A.V.; Bozorg SF, K.; Ojo, O.O. Evolution of solidification and microstructure in laser-clad IN625 superalloy powder on GTD-111 superalloy. *Surf. Coat. Technol.* **2021**, *412*, 127010. [CrossRef]
20. Liu, Y.; Li, C.X.; Huang, X.F.; Zhang, H.Y.; Li, C.J. Investigation on solidification structure and temperature field with novel processing of synchronous powder-feeding underwater laser cladding. *J. Mater. Process. Technol.* **2021**, *296*, 117166. [CrossRef]

21. Liu, J.; Sun, W.; Huang, Y. Effect of carbon nanotubes content on microstructure and properties of WC/Ni laser cladding coatings. *Surf Eng.* **2020**, *37*, 650–657. [CrossRef]
22. Gorunov, A.I.; Gilmutdinov, A.K. Investigation of coatings of austenitic steels produced by supersonic laser deposition. *Opt. Laser Technol.* **2017**, *88*, 157–165. [CrossRef]
23. Xu, X.; Lu, H.F.; Luo, K.Y.; Yao, J.H.; Xu, L.Z.; Lu, J.Z.; Lu, Y.F. Mechanical properties and electrochemical corrosion resistance of multilayer laser cladded Fe-based composite coatings on 4Cr5MoSiV1 steel. *J. Mater. Process. Technol.* **2020**, *284*, 116736. [CrossRef]
24. Cladera, A.; Weber, B.; Leinenbach, C.; Czaderski, C.; Shahverdi, M.; Motavalli, M. Iron-based shape memory alloys for civil engineering structures: An overview. *Constr. Build. Mater.* **2014**, *63*, 281–293. [CrossRef]
25. Fu, Z.K.; Ding, H.H.; Wang, W.J.; Liu, Q.Y.; Guo, J.; Zhu, M.H. Investigation on microstructure and wear characteristic of laser cladding Fe-based alloy on wheel/rail materials. *Wear* **2015**, *330–331*, 592–599. [CrossRef]
26. Yuan, W.; Li, R.; Chen, Z.; Gu, J.; Tian, Y. A comparative study on microstructure and properties of traditional laser cladding and high-speed laser cladding of Ni45 alloy coatings. *Surf. Coat. Technol.* **2021**, *405*, 126582. [CrossRef]
27. Assadi, H.; Kreye, H.; Gärtner, F.; Klassen, T. Cold spraying—A materials perspective. *Acta Mater.* **2016**, *116*, 382–407. [CrossRef]
28. Yakhot, V. Renormalization group analysis of turbulence: Basic theory. *J. Sci. Comput.* **1986**, *1*, 3–51. [CrossRef]
29. Chang, C.M.; Lin, C.M.; Hsieh, C.C.; Chen, J.H.; Wu, W. Micro-structural characteristics of Fe–40wt%Cr–xC hardfacing alloys with [1.0–4.0wt%] carbon content. *J. Alloys Compd.* **2009**, *487*, 83–89. [CrossRef]
30. Yao, J.; Yang, L.; Li, B.; Li, Z. Characteristics and performance of hard Ni60 alloy coating produced with supersonic laser deposition technique. *Mater. Des.* **2015**, *83*, 26–35. [CrossRef]
31. Gu, D.D.; Meiners, W.; Wissenbach, K.; Poprawe, R. Laser additive manufacturing of metallic components: Materials, processes and mechanisms. *Int. Mater. Rev.* **2013**, *57*, 133–164. [CrossRef]
32. Gu, D.; Hagedorn, Y.C.; Meiners, W.; Meng, G.; Batista RJ, S.; Wissenbach, K.; Poprawe, R. Densification behavior, microstructure evolution, and wear performance of selective laser melting processed commercially pure titanium. *Acta Mater.* **2012**, *60*, 3849–3860. [CrossRef]
33. Attar, H.; Calin, M.; Zhang, L.C.; Scudino, S.; Eckert, J. Manufacture by selective laser melting and mechanical behavior of commercially pure titanium. *Mater. Sci. Eng. A* **2014**, *593*, 170–177. [CrossRef]
34. Masanta, M.; Shariff, S.M.; Choudhury, A.R. Evaluation of modulus of elasticity, nano-hardness and fracture toughness of TiB_2–TiC–Al_2O_3 composite coating developed by SHS and laser cladding. *Mater. Sci. Eng. A* **2011**, *528*, 5327–5335. [CrossRef]
35. Kalyanasundaram, D.; Molian, P. Electrodeposition of nanodiamond particles on aluminium alloy A319 for improved tribological properties. *Micro Nano Lett.* **2008**, *3*, 110. [CrossRef]
36. Shi, X.; Wen, D.; Wang, S.; Wang, G.; Zhang, M.; Li, J.; Xue, C. Investigation on friction and wear performance of laser cladding Ni-based alloy coating on brake disc. *Optik* **2021**, *242*, 167227. [CrossRef]
37. Liu, Q.; Pang, M.; Chen, J.; Liu, G.; Zhang, L. Microstructure and properties characterization of Ti-containing Ni60/Graphite self-lubricating composite coatings applied on 300M ultra-high strength steel by laser cladding. *Mater. Chem. Phys.* **2021**, *266*, 124554. [CrossRef]
38. Wang, Q.; Yang, J.; Niu, W.; Li, Y.; Mao, X.; Wang, Y.; Zhang, K. Effect of La_2O_3 on microstructure and properties of Fe-based alloy coatings by laser cladding. *Optik* **2021**, *245*, 167653. [CrossRef]